Journal of Nanobiotechnology

RESEARCH Open Access

Transformable self-delivered supramolecular nanomaterials combined with anti-PD-1 antibodies alleviate tumor immunosuppression to treat breast cancer with bone metastasis

Xueying Liu[1†], Hao Wang[3†], Zhaofeng Li[1†], Jiamei Li[2], Siqin He[2], Chuan Hu[2], Yujun Song[2], Huile Gao[2*] and Yi Qin[1*]

Abstract

Breast cancer is the most common malignant tumor that threatens women's life and health, and metastasis often occurs in the advanced stage of breast cancer, leading to pathological bone destruction and seriously reducing patient quality of life. In this study, we coupled chlorin e6 (Ce6) with mono-(6-amino-6-deoxy)-beta-cyclodextrin (*β*-CD) to form Ce6-CD, and combined ferrocene with the $FFVLG_3C$ peptide and PEG chains to form the triblock molecule Fc-pep-PEG. In addition, the IDO-1 inhibitor NLG919 was loaded with Ce6-CD and Fc-pep-PEG to construct the supramolecular nanoparticle NLG919@Ce6-CD/Fc-pep-PEG (NLG919@CF). After laser irradiation, Ce6 produced robust reactive oxidative species to induce tumor cell apoptosis. Simultaneously, ferrocene became charged, and Fc-pep-PEG dissociated from the spherical nanoparticles, enabling their transformation into nanofibers, which increased both the retention effect and the induction of ferroptosis. The released NLG919 reduced the number of regulatory T cells (Tregs) and restored the function of cytotoxic T lymphocytes (CTLs) by inhibiting the activity of IDO-1. Moreover, combined administration with an anti-PD-1 antibody further relieved immune suppression in the tumor microenvironment. This article presents a new strategy for the clinical treatment of breast cancer with bone metastasis and osteolysis.

Keywords Photodynamic therapy, IDO-1, PD-1, Shape transformation, Breast cancer with bone metastasis

[†]Xueying Liu, Hao Wang and Zhaofeng Li contributed equally to this work.

*Correspondence:
Huile Gao
gaohuile@scu.edu.cn
Yi Qin
qinyi0225@163.com

Full list of author information is available at the end of the article

Graphical Abstract

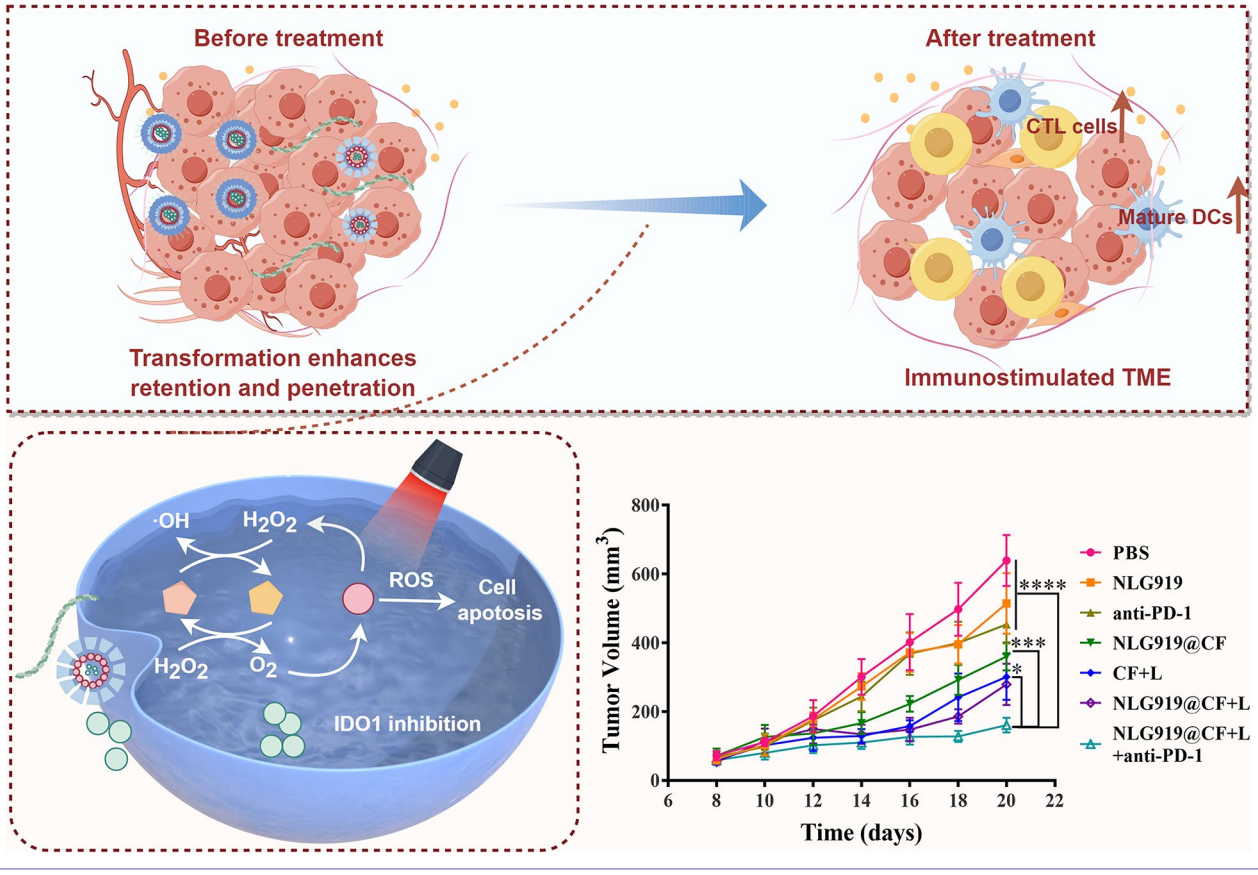

Introduction

Breast cancer, which ranks first and second in incidence and mortality, respectively, among female malignant tumors, threatens the life and health of women worldwide [1]. Bone is the most susceptible site to breast cancer metastasis [2]. Studies have shown that the interaction of breast cancer cells with bone metastases and osteoblasts further increases the ability of breast cancer cells to invade, metastasize, and grow, which accelerates multiorgan metastasis throughout the body [3, 4]. At present, the treatment methods for breast cancer bone metastases mainly include surgery, radiotherapy and chemotherapy, which can alleviate bone metastasis to a certain extent. However, these traditional therapies have many shortcomings, such as high trauma, high risk, and in case of surgical treatment, numerous postoperative complications. Radiotherapy and chemotherapy can induce toxic side effects, such as bone marrow suppression [5], and can cause massive bone loss [6]. Therefore, exploring new strategies for the treatment of breast cancer with bone metastasis is highly important for improving patient survival and quality of life.

Photodynamic therapy (PDT) is an emerging minimally invasive treatment in which large amounts of cytotoxic reactive oxygen species (ROS) are produced by laser irradiation via photosensitizers, resulting in selective cytotoxicity and immunogenic cell death (ICD) to malignant cells [7]. However, the therapeutic efficacy of PDT is limited by the complexity of the tumor microenvironment. First, the tumor microenvironment of breast cancer is hypoxic, which weakens the photodynamic effect of oxygen dependence [8]. In addition, the oxygen-consuming properties of PDT exacerbate tumor hypoxia, forming a vicious cycle [9]. Both the hypoxic environment of tumors and the limited light penetration depth of lasers limit ROS production in PDT. One effective strategy to intensify the effect of PDT is chemical dynamic therapy (CDT) based on the Fenton reaction. Catalyzed by Fe^{2+}/Fe^{3+} ions, the Fenton reaction converts endogenous H_2O_2 into ·OH, which is a highly toxic ROS. The reaction can also produce O_2, thereby increasing the therapeutic effect of PDT [10]. The H_2O_2 produced during PDT can also be used as a substrate for CDT, forming a positive cycle [11]. Second, tumors express immune checkpoints such as programmed cell death receptor ligand 1 (PD-L1) and

indolamine 2,3-dioxygenase-1 (IDO-1) to establish an immunosuppressive microenvironment [12, 13], resulting in T-cell dysfunction in tumor recognition and killing. Unsurprisingly, tumor immune escape can restrict the therapeutic efficacy of PDT. Therefore, combining PDT with CDT, IDO-1 inhibitors and anti-PD-1 antibodies is an effective approach to tumor treatment.

However, achieving the efficient and low-toxicity codelivery of multiple drugs in vivo remains an enormous challenge. In recent years, nanodrug delivery systems composed of photosensitizers have attracted increasing attention. Nanoparticles are enriched at tumor sites through the enhanced permeability and retention (EPR) effect. However, due to the densification of tumor tissues and high interstitial pressure, nanoparticles cannot easily permeate tumor tissues and are quickly cleared, limiting their therapeutic efficacy [14]. Studies have shown that changing the physical properties of nanoparticles, such as their size [15] and shape [16], can promote their delivery to tumors. For example, spherical nanoparticles penetrate tumors effectively but are easily removed from tumor tissue due to poor retention. Nanofibers are more effectively retained, but their deep penetration ability is poor [17–19]. Therefore, tumor site-responsive transformable nanoparticles can be constructed to increase the efficiency of drug delivery.

In this study, we designed the transformable self-delivered supramolecular nanoparticle NLG919@CF for PDT (Scheme 1). We first linked the photosensitizer chlorin e6 (Ce6) with β-cyclodextrin (β-CD) to synthesize Ce6-CD and combined ferrocene (Fc) with the $FFVLG_3C$ peptide and PEG chains to form the triblock molecule Fc-pep-PEG. Fc was used as the guest molecule, and β-CD was the host molecule. Together with NLG919, an IDO-1 inhibitor, we constructed the supramolecular nanoparticle NLG919@CF. The ROS generated by PDT oxidize Fc to Fc^+ so that Fc-pep-PEG can detach from the hydrophobic cavity of Ce6-CD and further form nanofibers to increase its retention. In addition, nanoparticles loaded with NLG919 reduced the number of regulatory T cells (Tregs) and restored the function of cytotoxic T lymphocytes (CTLs). The incorporation of an anti-PD-1

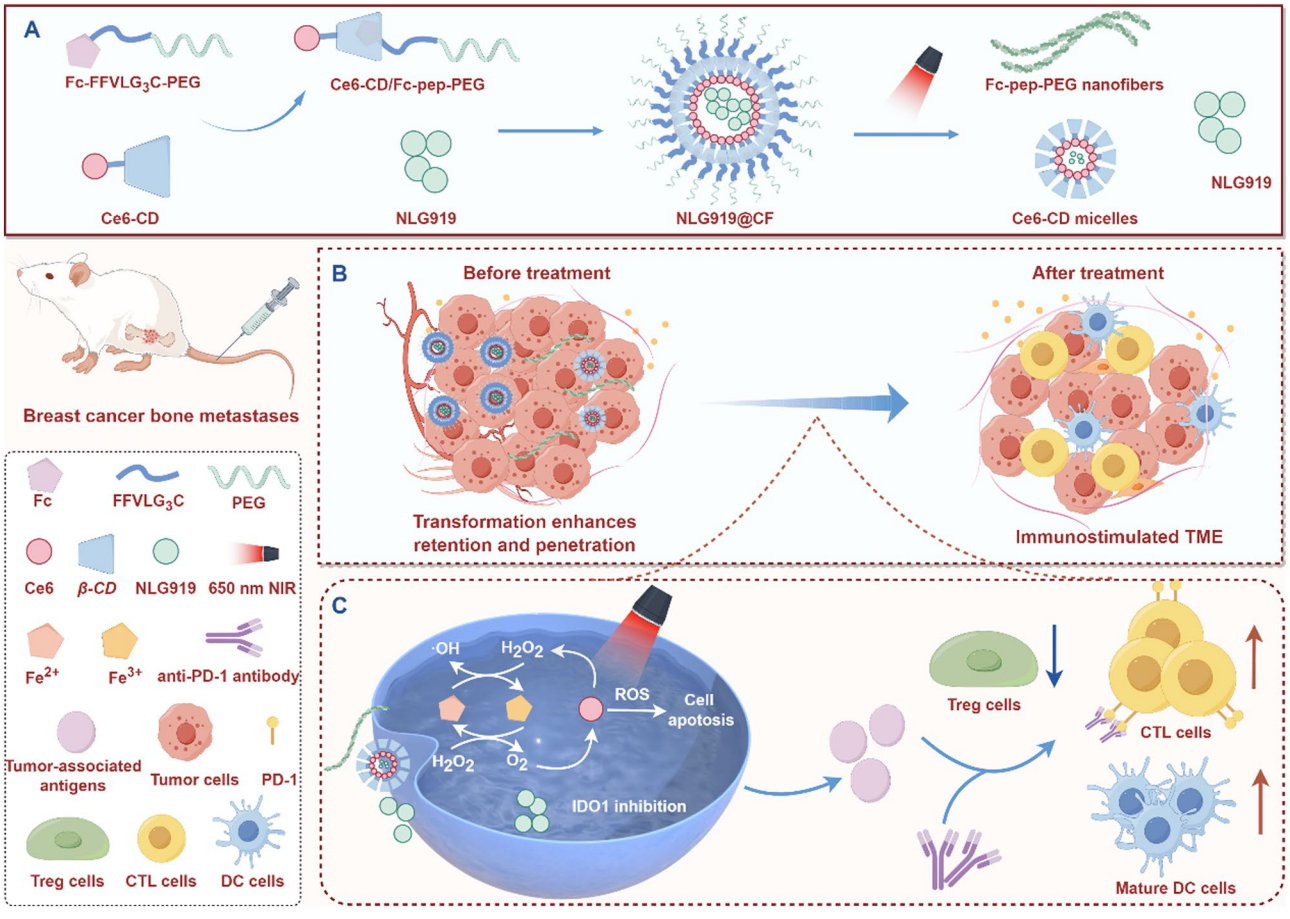

Scheme 1 **A**) Fabrication of the transformable self-delivered supramolecular nanomaterial NLG919@CF though host–guest complexation between Ce6-CD and Fc-pep-PEG. **B**) Schematic illustration of local immune microenvironment changes in tumors before and after treatment. **C**) Schematic illustration of the mechanism of NLG919@CF combined with an anti-PD-1 antibody in the coordinated treatment of tumors

antibody further relieved the inhibition of T cells and restored their vitality. This study is expected to provide new insights for the treatment of breast cancer bone metastases.

Results and discussion

Synthesis and characterization of NLG919@CF

According to the research methods explored by our group [20] in the early stage, we synthesized Fc-pep-PEG and Ce6-CD. The peaks measured by matrix-assisted laser desorption/ionization time-of-flight mass spectrometry (MALDI-TOF-MS) at approximately m/z 974.66, 1007.37 and 2068.09 were attributed to $mPEG_{1000}$-Mal, Fc-FFVLG_3C and Fc-FFVLG_3C-$mPEG_{1000}$, respectively (Figure S1A-C). The proton nuclear magnetic resonance (^{1}HNMR) spectra of Fc-pep-PEG showed the critical peaks around δ_H 7.21 and δ_H 3.41, which were attributed to phenylalanine and PEG chains, respectively (Figure S2A, B). These results indicated the successful synthesis of Fc-pep-PEG. The peak measured by MALDI-TOF-MS at approximately *m/z* 1695.78 was attributed to Ce6-CD (Figure S1D). The characteristic peaks of Ce6 and β-CD mainly appeared at 3-6ppm and 8-10ppm respectively also appeared in Ce6-CD (Figure S2C-E), indicating the successful synthesis. The infrared spectrum results showed an absorption peak of C=O at 1715 cm^{-1} attributing to Ce6-CD, while the raw material *β*-CD did not have the peak, which also indicated the successful synthesis of Ce6-CD (Figure S3A). After the ultrasonic treatment of Fc-pep-PEG and Ce6-CD, the characteristic peak of ferrocene ring at around 2800 cm^{-1} was weaker than that of mechanical mixing, indicating the formation of supramolecular inclusion complex (Figure S3B).

Subsequently, the nanoparticles were prepared by the solvent diffusion method, and their size, potential and morphology were characterized. As shown in Fig. 1A, the average size of the NLG919@CF was 90.3±2.8 nm, and the PDI was 0.171±0.027, indicating that the NLG919@

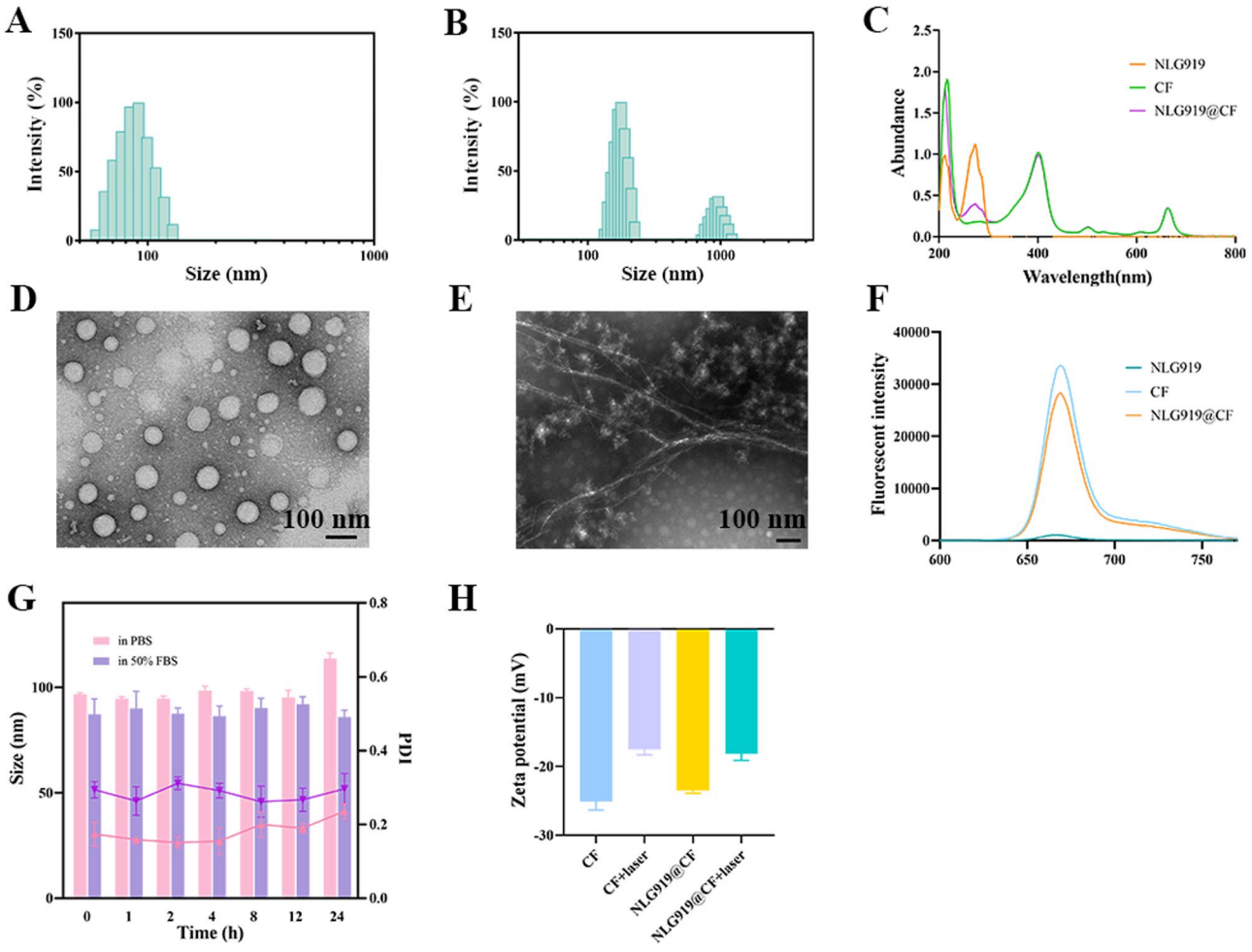

Fig. 1 Characterization of nanomedicines. Particle size images of (**A**) NLG919@CF and (**B**) NLG919@CF + laser. (**C**) Ultraviolet absorption spectra of NLG919, CF and NLG919@CF. TEM images of (**D**) NLG919@CF and (**E**) NLG919@CF + laser. (**F**) Fluorescence spectra of NLG919, CF and NLG919@CF. (**G**) Stability of NLG919@CF in PBS and 50% FBS. (**H**) Zeta potentials of the different nanoparticles

CF had a relatively uniform size and distribution. Fc^{+}-pep-PEG separated from Ce6-CD after 650 nm laser irradiation and then formed larger nanofibers (Fig. 1B). Through transmission electron microscopy, we verified that laser irradiation transformed the nanoparticles from spherical to nanofibrous particles (Fig. 1D, E). The ultraviolet absorption spectrum (Fig. 1C) showed that characteristic absorption peaks of Ce6 (404 nm, 668 nm) and NLG919 (274 nm) appeared in the absorption spectrum of NLG919@CF, indicating that the construction of the drug-loaded nanoparticles was successful. Similarly, the fluorescence spectroscopy emission peak position results again illustrated the successful construction of NLG919@CF (Fig. 1F). The lack of a significant change in the particle size of the nanoparticles in PBS (pH=7.4) or 50% FBS indicated the good stability of the nanoparticles (Fig. 1G). Finally, we measured the zeta potentials of the different nanoparticles. The results showed that the surface zeta potentials of CF and NLG919@CF increased from −14.96±0.62 mV and −11.63±0.71 mV to -12.64±0.45 mV and −10.07±0.84 mV, respectively, after laser irradiation, indirectly verifying that Fc was oxidized by ROS to a water-soluble charged form (Fig. 1H).

Cellular uptake and retention in vitro

First, we qualitatively observed the uptake of nanoparticles in cells by laser confocal microscopy. There was no significant difference in the red fluorescence intensity of the CF or NLG919@CF nanoparticles, but both of them were stronger than those in the free Ce6 group. The uptake of nanoparticles by 4T1 cells was time-dependent (Fig. 2A). Quantitative measurement of nanoparticle uptake by flow cytometry yielded similar results. After 4 h of incubation, the fluorescence intensity of the NLG919@CF group was 1.61 times greater than that of the free Ce6 group (Fig. 2B, Figure S4A). The results above showed that the nanoparticles we prepared could promote the uptake of Ce6 by 4T1 cells. Some studies have shown that nanofibers are more likely to be taken up by cells than spherical nanoparticles [19, 21], therefore, we labeled Fc-PEP-PEG fragments with FITC to validate this possibility through flow cytometry and confocal imaging. After laser irradiation, the spherical nanoparticles were transformed into nanofibers, and the intensity of the green fluorescence in the laser irradiation group was significantly greater than that in the nonirradiated group (Fig. 2C). Flow cytometry quantification revealed that the fluorescence intensity of the laser-irradiated group was 2.47-fold greater than that of the nonirradiated group (Fig. 2D, Figure S4B). Finally, we used multicellular spheroids (MSCs) to investigate the retention of the nanomedicines. After 4 h of treatment, the culture medium of the MSCs was replaced with fresh drug-free culture medium, and the laser-on group was irradiated with the laser. After the MSCs were cultured for another 4 h, the fluorescence intensity of the laser irradiation group was greater than that of the nonirradiated group at a scanning depth of 40–70 μm (Fig. 2E). In conclusion, these results demonstrated that, compared with spherical nanoparticles, nanofibers were more easily taken up by 4T1 cells and more effectively retained.

ROS generation and cytotoxicity in vitro

ROS production plays a key role in tumor cell damage during PDT. Therefore, we investigated the ROS production ability of NLG919@CF by ROS Assay Kit. In the absence of laser irradiation, the green fluorescence intensity of ROS in the drug group was weak, and was almost the same as that of the blank group. After 20 s of laser irradiation, we observed fluorescence enhancement of ROS in the free Ce6+L (+L represents with laser irradiation) group, CF+L group and NLG919@CF+L group, with CF+L group and NLG919@CF+L group significantly higher than that of the free Ce6+L group (Fig. 3A). Flow cytometry showed that ROS production in the NLG919@CF+L group was 3.09 times higher than that in NLG919@CF group, and was 2.76 times higher than that in the Ce6+L group (Fig. 3B, Figure S4C).

To evaluate the cytotoxicity of the nanoparticles, we first used Annexin V-FITC/PI double staining to quantitatively investigate the induction of apoptosis in 4T1 cells by NLG919@CF. The results showed that after laser irradiation, the proportions of early apoptotic, late apoptotic and necrotic cells in the CF+L group and NLG919@CF group increased significantly. The proportions of late apoptotic cells in the CF+L group and NLG919@CF+L group were 2.80 times and 2.47 times higher than those in the free Ce6+L group, respectively, and the proportion of necrotic cells was 6.13 times higher than that in the free Ce6+L group (Fig. 3C, D). To visualize the efficacy of NLG919@CF in vitro, we stained 4T1 cells with calcein-AM/PI to distinguish live cells from dead cells. Confocal fluorescence microscopy revealed that the nonirradiated group exhibited strong green fluorescence. After laser irradiation, red fluorescence corresponding to PI was observed in both the free Ce6 group and the NLG919@CF group. In particular, only a small number of viable cells were observed in the NLG919@CF group (Fig. 3E), which further confirmed the effectiveness of PDT. Finally, the cytotoxicity of the nanoparticles to 4T1 cells was investigated by MTT. The results showed that the half-maximal inhibitory concentration (IC_{50}) in the NLG919@CF+L group was 0.21 μg/mL, which was almost the same as that in the CF+L group (0.21 μg/mL), and lower than that in the free Ce6+L group (0.62 μg/mL) (Fig. 4A). These findings indicated that the NLG919@CF nanoparticles had stronger cytotoxic effects than free Ce6 after laser irradiation. Taken together, these results showed

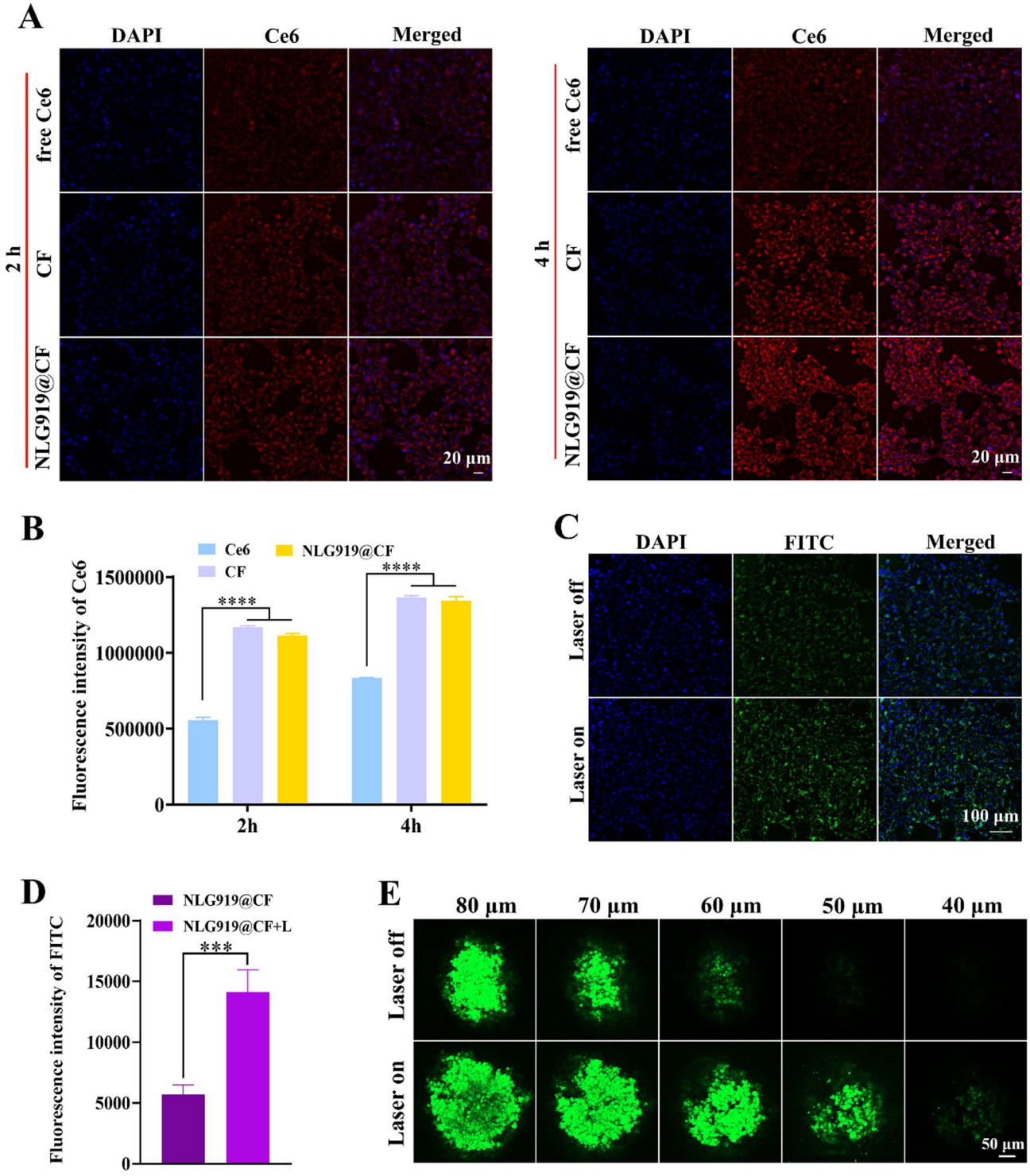

Fig. 2 Cellular uptake and retention in vitro. Cellular uptake of the nanomedicine was observed by **A**) confocal microscopy and evaluated by **B**) flow cytometry. **C**) Confocal microscopy and **D**) flow cytometry showed that after laser irradiation, tumor cells exhibited enhanced absorption and retention of the nanomedicine. E) Confocal image of 4T1 tumor spheres incubated with NLG919@CF. (***$p < 0.001$, ****$p < 0.0001$)

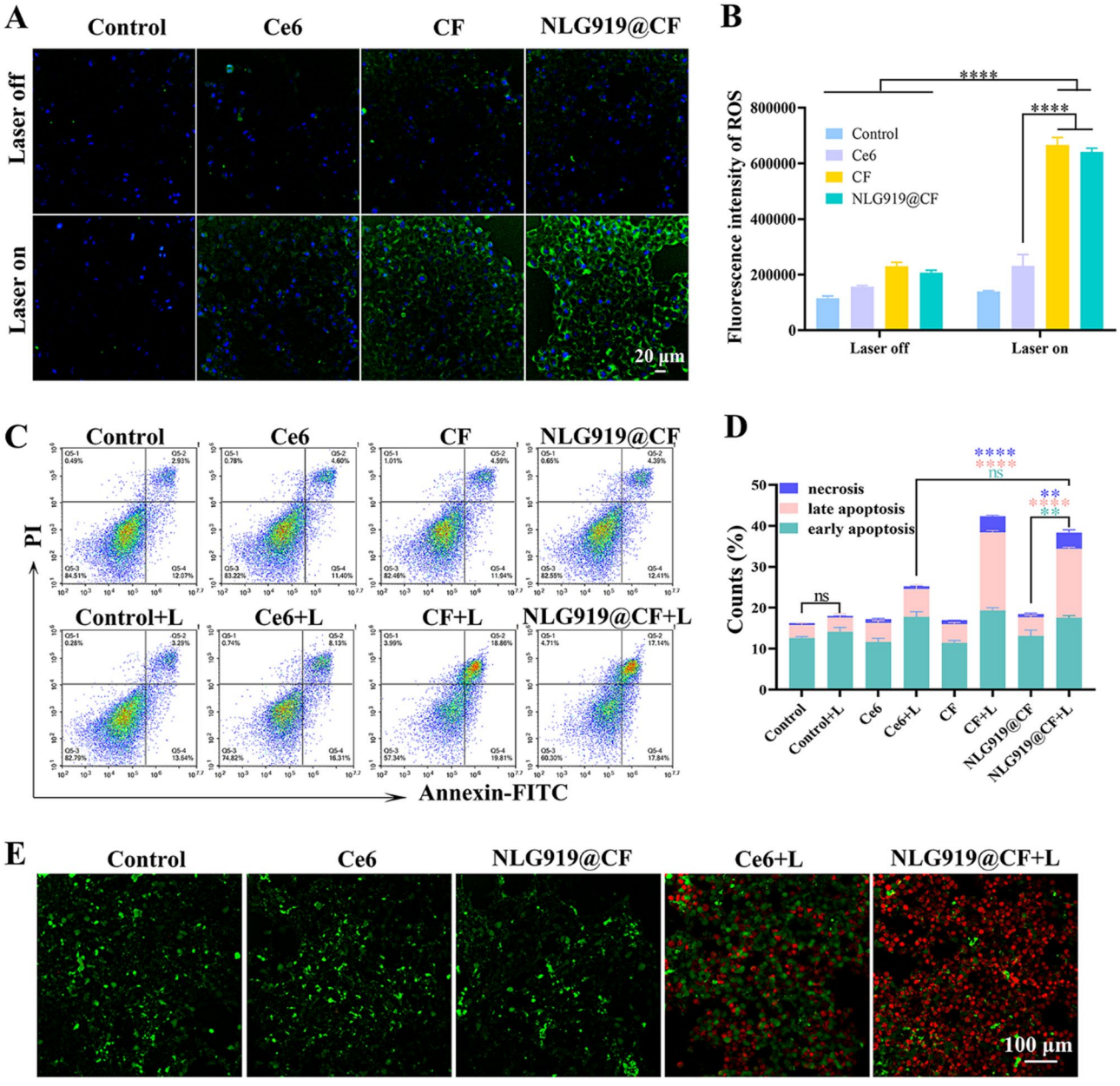

Fig. 3 ROS generation and cytotoxicity in vitro. **A**) The ROS generation ability of different formulations was observed by **A**) confocal microscopy using ROS Assay Kit (blue represents DAPI, green represents ROS) and **B**) flow cytometry through analyzing the mean fluorescence intensity of ROS. **C**) Apoptosis analysis of 4T1 cells treated with different formulations. **D**) Statistical analysis of the apoptosis results. E) Calcein-AM/PI double staining of 4T1 cells treated with different formulations. (**$p < 0.01$, ****$p < 0.0001$)

that Fc promoted the cytotoxicity of Ce6+L and further the PDT efficacy, while NLG919 had no obvious cytotoxicity at the corresponding concentration.

ICD induction in vitro

In recent years, many studies have shown that PDT can also lead to the efflux of calreticulin (CRT), secretion of adenosine triphosphate (ATP), and release of high-mobility group protein 1 (HMGB1), increasing the immunogenicity of tumor cells and activating antitumor immune responses [22–24]. Therefore, we investigated the ability of NLG919@CF to induce ICD production in 4T1 cells after laser irradiation. First, we detected the expression of CRT by flow cytometry. The results showed that the efflux of CRT in the NLG919@CF group, CF group and free Ce6 group was greater after laser irradiation (Fig. 4B, Figure S5). Confocal microscopy imaging provided similar results (Fig. 4E). HMGB1, a protein located in the nucleus, is expelled from the nucleus after tumor cells are stimulated by laser irradiation [25]. We measured

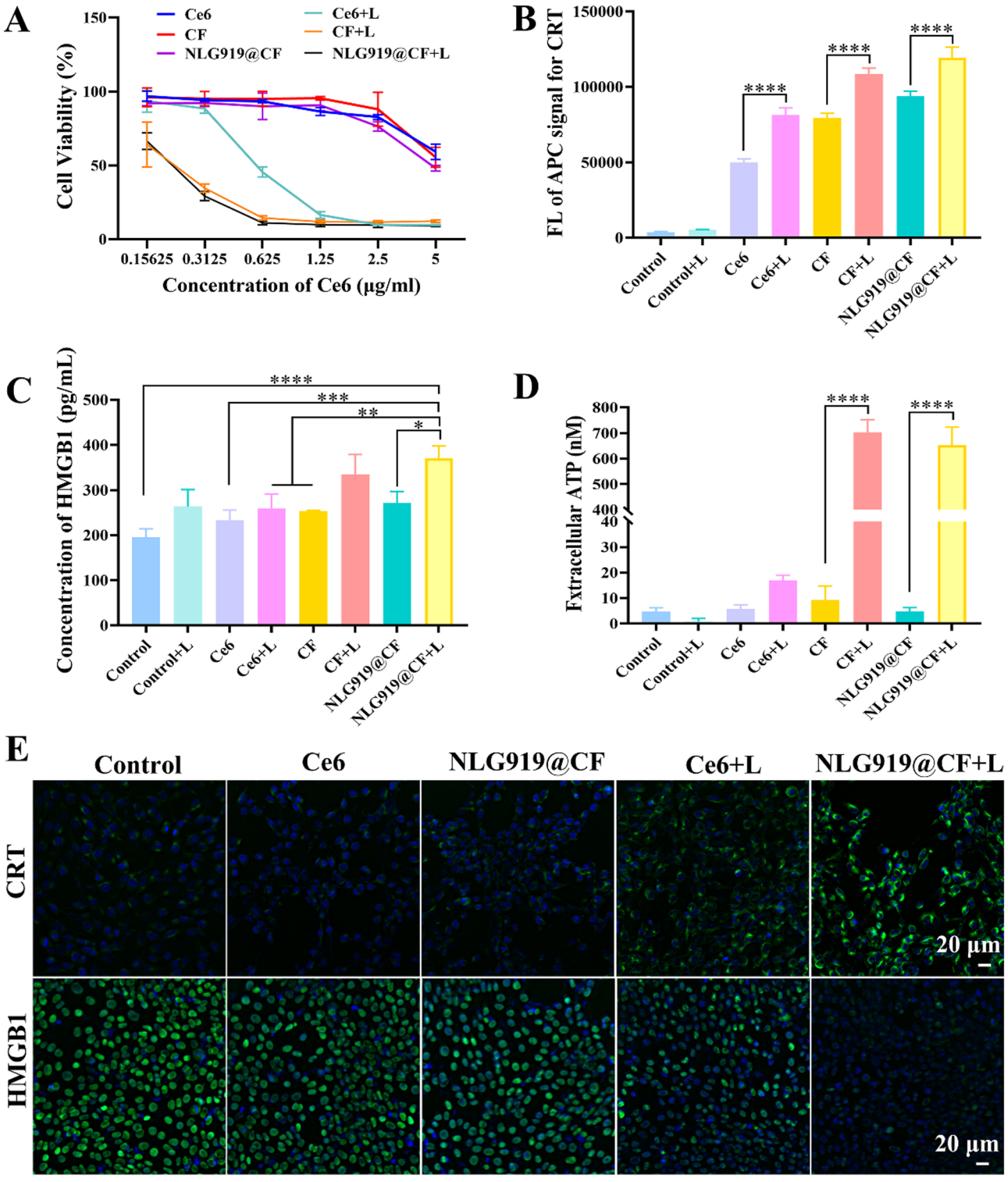

Fig. 4 **A**) The inhibitory effects of different formulations on the proliferation of 4T1 cells, determined by MTT assay. **B**) The ability of 4T1 cells treated with different formulations to produce CRT was determined by flow cytometry. **C**) ELISA assay of extracellular HMGB-1 release from 4T1 cells incubated with different formulations. **D**) Extracellular secretion of ATP. **E**) Confocal images of CRT and HMGB1 expression on the surface of 4T1 cells. (*$p < 0.05$, **$p < 0.01$, ***$p < 0.001$, ****$p < 0.0001$)

the secretion of HMGB1 in the extracellular space by an enzyme-linked immunosorbent assay and the level of intracellular HMGB1 by confocal microscopy imaging. The results showed that the secretion of HMGB1 from the cells increased in the dosing group after laser irradiation, with the secretion in the NLG919@CF+L group being 1.36 times higher than that in the NLG919@CF group (Fig. 4C), while the intracellular retention of HMGB1 decreased correspondingly (Fig. 4E). Figure 4D shows that the secretion of ATP in the dosing group increased significantly after laser irradiation, and that in the NLG919@CF+L group was 134.6 times higher than that in the NLG919@CF group.

Biodistribution and retention evaluation in vivo

A 4T1 breast tumor model was constructed to evaluate the distribution and retention of the nanoparticles in vivo. First, fluorescence imaging of Ce6 was used to investigate the distribution of the nanoparticle CF in vivo after tail vein injection in mice. At 24 h post-administration, the CF group still had a strong tumor signal, while the free Ce6 group had a very weak signal, which indicated that the CF nanoparticles accumulated at the tumor site through the EPR effect, while free Ce6 was quickly metabolized and cleared from the body (Fig. 5A). Ex vivo imaging revealed that the fluorescence intensity at the tumor site in the CF group was 3.53 times greater than that in the free Ce6 group (Fig. 5B, C). Subsequently, similar results were obtained for frozen section of the isolated tissues (Fig. 5F, Figure S4A). The results above confirmed the high accumulation ability of the CF nanoparticles at the tumor site.

Then we evaluated the contribution of shape transformation to the retention of the nanoparticles in vivo. Ce6-CD/Fc-pep-PEG-FITC in the mouse tumor quickly subsided after 24 h without laser irradiation, while the laser irradiation group still had a strong signal of FITC (Figure S6B, C). Ex vivo imaging of the tumors, corresponding semiquantitative analysis, and tumor cryosections yielded similar results (Fig. 5D, E and G), confirming that nanoparticles could transform into nanofibers, thereby increasing retention at the tumor site.

Antitumor and antimetastatic performance in vivo

We combined PDT with an anti-PD-1 antibody and evaluated the antitumor effect. The results are shown in Fig. 6. Measuring the morphology, mass and volume of the tumors in each group at the end of treatment, it revealed that the tumor mass and volume were the smallest in the NLG919@CF+L+anti-PD-1 group (Fig. 6A-C), and the tumor growth trend was the slowest in this group (Figure S8A-G). After treatment with NLG919@CF (laser on) combined with anti-PD-1 antibody, the relative growth rate of the tumors decreased from 100% (PBS group) to 25.1%, and the relative growth rates of tumors in the remaining groups were 43.6% (NLG919@CF+L), 47.1% (CF+L), 56.4% (NLG919@CF), 71.0% (anti-PD-1), and 80.5% (NLG919). The combination of anti-PD-1 antibody with an IDO-1 inhibitor and PDT inhibited tumor growth more effectively. Bone metastases can lead to subsequent lung metastases [26]. Figure 6D and E and Figure S7 show that, compared with the PBS group, the NLG919@CF+L+anti-PD-1 group had significantly fewer lung pulmonary nodules, demonstrating that PDT combined with an anti-PD-1 antibody could also effectively inhibit lung metastasis.

We further used H&E and TUNEL staining to analyze tumor necrosis and apoptosis after treatment. As shown in Fig. 6F, tumor cells in the PBS group exhibited almost no necrosis or apoptosis, and there was a degree of necrosis and apoptosis in tumor cells from the CF+L and NLG919@CF+L groups, while large-scale necrosis and apoptosis was observed in tumor cells after treatment with NLG919@CF+L+anti-PD-1. Furthermore, the greatest antitumor effect was observed in the NLG919@CF+L+anti-PD-1 group. Subsequently, we investigated CRT efflux and HMGB1 expression in tumor cells via confocal imaging. The results showed that the expression of CRT and HMGB1 proteins was significantly increased on the surface of tumor cells after laser irradiation, indicating that PDT in vivo can induce ICD in tumor cells. Finally, for the safety evaluation of the nanoparticles in vivo, we evaluated weight changes during treatment, H&E staining of major organs at the end of treatment and routine blood and liver and kidney function test results. The results revealed no obvious histological damage in any of the treatment groups compared with the PBS group (Figures S8H, S9, S10). These results indicated that our constructed nanoparticles combined with an anti-PD-1 antibody and an IDO-1 inhibitor had satisfactory therapeutic efficacy and no obvious side effects.

Antitumor immunity

We investigated the immune status of each group after treatment by detecting the expression of surface costimulatory molecules produced by dendritic cells in the spleen and lymph nodes and the presence of CTLs and Tregs in tumor tissues. The $CD11c^+CD80^+$ cell subset (Fig. 7A, Figure S11) and $CD11c^+CD86^+$ cell subset (Fig. 7B, Figure S12) frequencies in the NLG919@CF+L group were 2.16 times and 1.82 times greater than those in the NLG919@CF group, respectively, suggesting that Ce6-mediated PDT can induce dendritic cell maturation in the spleen. Moreover, there was no significant difference between the CF+L group and the NLG919@CF+L group, indicating that NLG919 had no significant effect on the maturation of DC cells. Among all the groups, the percentages of $CD11c^+CD80^+$ and $CD11c^+CD86^+$

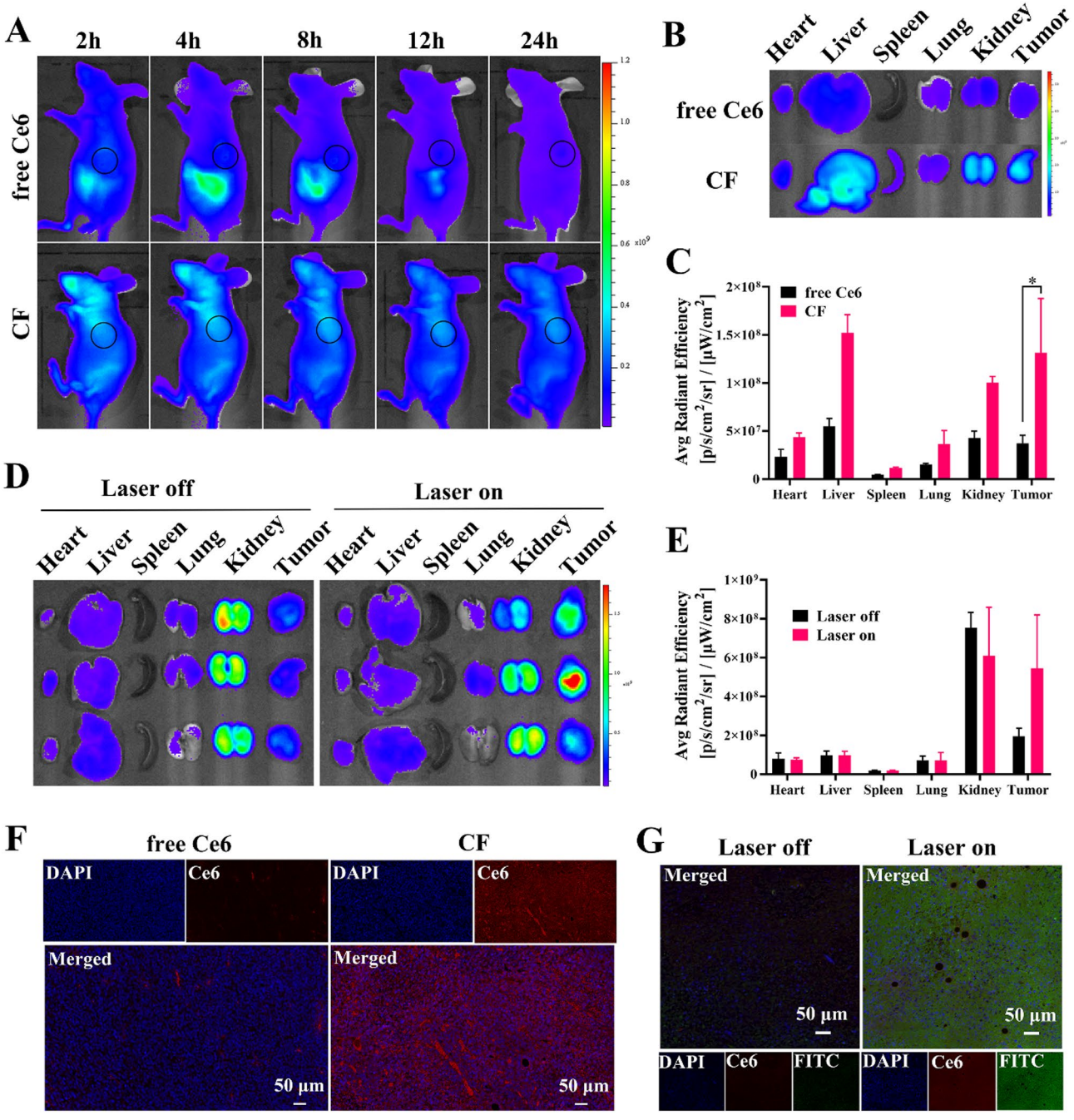

Fig. 5 Evaluation of biodistribution and retention in vivo in 4T1 tumor-bearing nude BALB/c mice. **A**) In vivo fluorescence imaging of mice at 2 h, 4 h, 8 h, 12 h and 24 h after tail vein administration of free Ce6 and CF. The sites circled in black are tumor sites. **B**) In vitro fluorescence imaging of major organs and tumors 24 h after tail vein administration. **C**) Semiquantitative statistical analysis of in vitro fluorescence of major organs and tumors 24 h after tail vein administration. **D**) In vitro fluorescence imaging of major organs and tumors in mice 24 h after intratumoral injection of Ce6-CD/Fc-pep-PEG-FITC. **E**) Semiquantitative statistical analysis of in vitro fluorescence of major organs and tumors 24 h after intratumoral injection ($n = 3$, $^*p < 0.05$). **F**) Fluorescence distribution in frozen sections of tumors 24 h after tail vein administration of free Ce6 and CF. **G**) Fluorescence distribution in frozen sections of tumors 24 h after intratumoral injection of Ce6-CD/Fc-pep-PEG-FITC

cells in the NLG919@CF+L+anti-PD-1 subgroup were the highest, with values of 11.24% and 9.13%, respectively. These values were 3.50 and 3.08 times greater than those observed in the PBS group, indicating that treatment with NLG919@CF+L+anti-PD-1 effectively induced dendritic cell maturation in vivo. Similar results were obtained from the examination of DC maturation in lymph nodes (Fig. 7C, Figure S13). After DCs mature, they can activate naive T cells to become CTLs with tumor killing-functions. We analyzed CTL ($CD3^+CD8^+$)

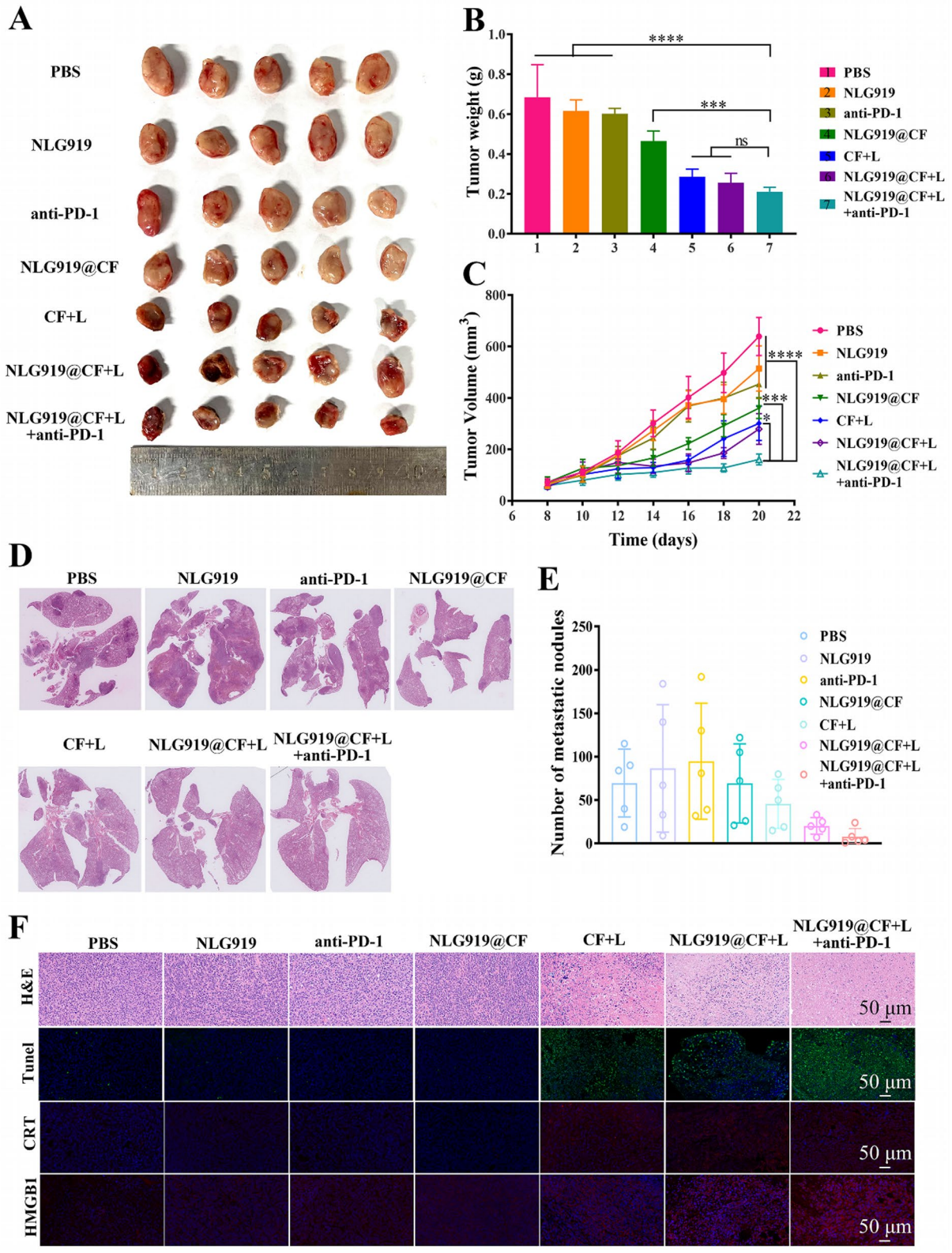

Fig. 6 Antitumor and antimetastatic effects in vivo. **A**) tumor image, **B**) tumor weight, and **C**) tumor growth curve of mice in different groups. **D**) H&E staining imaging of lungs after dissection of mice in different groups. **E**) The number of lung metastases in each group. **F**) H&E staining, TUNEL staining, CRT staining and HMGB1 staining of paraffin sections of tumors. (*$p < 0.05$, ***$p < 0.001$, ****$p < 0.0001$)

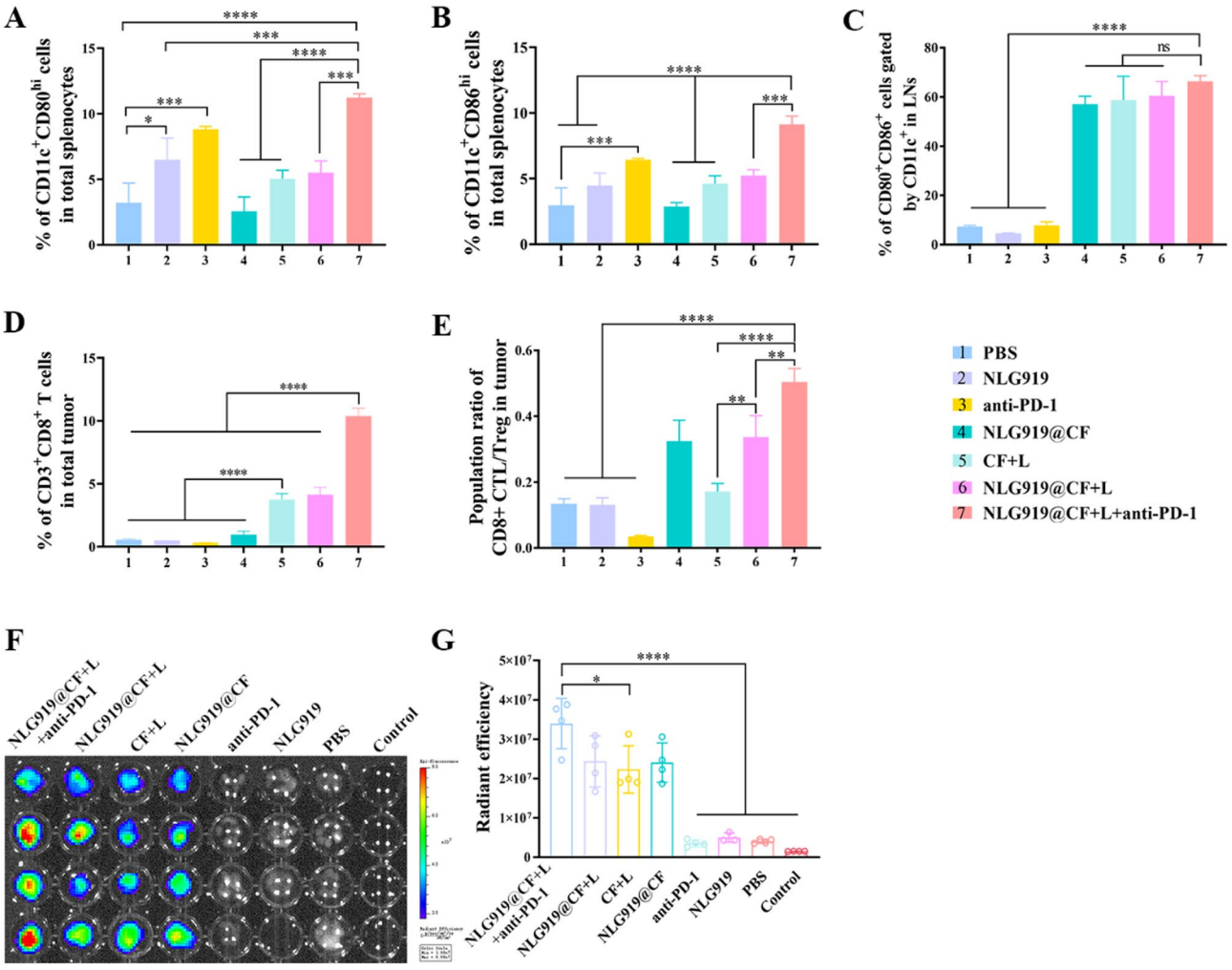

Fig. 7 Antitumor immunity in vivo. Flow cytometry analysis of **A**) $CD11c^+CD80^+$ cells and **B**) $CD11c^+CD86^+$ cells in the spleens of mice bearing primary tumor and bone metastases in different groups. **C**) Flow cytometry analysis of $CD80^+CD86^+$ cells in the lymph nodes. **D**) Flow cytometry analysis of CTLs and **E**) the ratio of CTL/Treg cells in primary tumors. **F**) Fluorescence imaging in vitro and corresponding **G**) semiquantitative fluorescence analysis of lymph nodes in different groups. (*$p < 0.05$, **$p < 0.01$, ***$p < 0.001$, ****$p < 0.0001$)

cells in tumor tissues and found that the number of CTLs in the NLG919@CF+L group was 4.33 times greater than that in the NLG919@CF group. The number of CTLs in the NLG919@CF+L+anti-PD-1 group was 19.21 times higher than that in the PBS group and 2.51 times higher than that in the NLG919@CF+L group (Fig. 7D, Figures S14 and S15). These results demonstrated that PDT combined with anti-PD-1 antibodies and IDO-1 inhibitors significantly increased the number of CTLs. In addition, the protocol increased the CTL/Treg ratio (Fig. 7E), indicating that the body produced a positive antitumor immune response.

We further dissected the mouse lymph nodes, imaged them ex vivo and performed semiquantitative analysis by imaging (Fig. 7F, G). NLG919@CF+L+anti-PD-1 had a higher lymphatic return effect than the other groups, and its fluorescence value was 8.36 times higher than that of the PBS group. Lymph nodes travel along the arteries and veins, buried in fat. Therefore, it is usually difficult to accurately identify them by the naked eye during surgery. After treatment according to our scheme, the lymph nodes were black and visible to the naked eye and could be traced by the imager, which could guide the clinical surgical removal of the lymph nodes.

Evaluation of osteolysis inhibition in vivo

To observe the erosion and destruction of the tibial bone in each group after treatment, the tibial tumor was peeled off after the treatment. The results demonstrated that the bone metastases in the NLG919@CF+L+anti-PD-1 group were the smallest (Fig. 8A), and the average weight was the lightest (Fig. 8B). Its average weight was 65.97% of free NLG919 group and 62.87% of anti-PD-1 group. The tibias of the mice in each group were

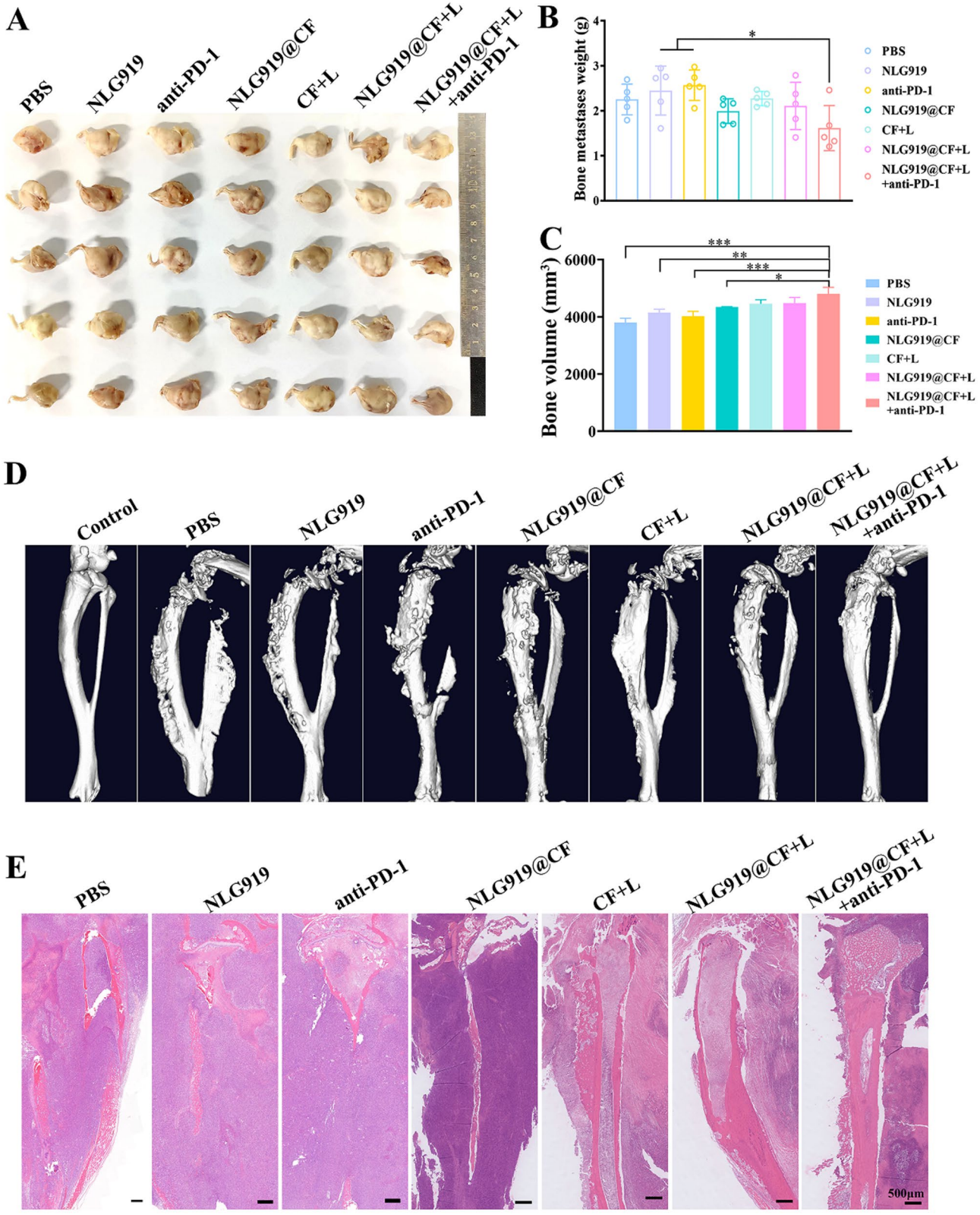

Fig. 8 Evaluation of osteolysis inhibition in vivo. **A**) Images of bone metastasis in the different groups. **B**) Bone metastasis weight. **C**) Bone volume and **D**) micro-CT reconstruction images and **E**) H&E staining of bone metastases in the different groups

subsequently evaluated via micro-CT and reconstructed in three dimensions. The results showed obvious bone destruction at the proximal tibia in the PBS group, free NLG919 group, anti-PD-1 group and NLG919@CF group, resulting in pathological comminuted fracture and bone nonunion. In the NLG919@CF+L+anti-PD-1 group, although an osteolytic destruction area could also be observed, the entire tibia was still continuous, and the bone defect area was significantly smaller than that in the other groups (Fig. 8D). The quantitative analysis of bone volume parameters measured by micro-CT showed that the average tibial volume in the NLG919@CF+L+anti-PD-1 group was the largest among all the groups, and was 1.26 times greater than that in the PBS group (Fig. 8C). Similar results were obtained by H&E staining and TRAP staining of mouse tibias (Fig. 8E). The results of TRAP staining showed that there were a number of osteoclasts in PBS group and monotherapy group, while the osteoclasts in NLG919@CF+L+anti-PD-1 group was significantly reduced (Figure S16). All the results above indicate that PDT combined with anti-PD-1 antibody therapy can effectively inhibit bone metastasis and reduce bone destruction.

Materials and methods

Materials

Ce6 was purchased from J&K Scientific Ltd. (Beijing, China). Mono-(6-amino-6-deoxy)-beta-cyclodextrin was purchased from Zhiyuan Biotechnology Ltd. (Shandong, China). NLG919 was purchased from Shanghai Maclean Biochemical Technology Co., Ltd. The peptide Fc-FFVLG$_3$C with ferrocene was purchased from Sangon Biotech Co., Ltd. (Shanghai, China). mPEG$_{1000}$-Mal and FITC-PEG$_{1000}$-Mal were purchased from Ponsure Biotechnology Co., Ltd. (Shanghai, China). Anti-PD-1 antibodies were purchased from Bioxcell. The Annexin V-FITC Apoptosis Detection Kit, Calcein/PI Cell Viability/Cytotoxicity Assay Kit, ROS Assay Kit and ATP Assay Kit were purchased from Beyotime Biotech Inc. (Shanghai, China). Anti-CRT antibodies, anti-HMGB1 antibodies, anti-CD11c antibodies and anti-CD8 antibodies were purchased from Abcam.

Cell lines and animals

Murine 4T1 breast cancer cells were obtained from the Chinese Academy of Sciences Cell Bank (Shanghai, China). 4T1 cells were cultured in 1640 medium supplemented with 10% fetal bovine serum and 1% penicillin-streptomycin solution and placed in a CO_2 incubator (5% CO_2, 37 °C). Female BALB/c mice (6–8 weeks, 20±2 g) were purchased from SpePharm Biotechnology Co., Ltd. (Beijing, China). All animal experiments were conducted under established guidelines and evaluated and approved by the Ethics Committee of Sichuan University.

Synthesis and characterization of Ce6-CD and Fc-pep-PEG

When preparing Ce6-CD, Ce6 was first activated. Ce6 (0.03 mmol, 18.00 mg), EDC (0.06 mmol, 11.50 mg) and DMAP (0.03 mmol, 3.67 mg) were dissolved in 2 mL of N, N-dimethylformamide (DMF) and stirred for 2 h at room temperature. Subsequently, mono-(6-amino-6-deoxy)-beta-cyclodextrin (β-CD) (0.01 mmol, 11.34 mg) was dissolved in 1 mL of DMF, and added to the activated Ce6. The mixture was stirred for 24 h. Finally, the obtained product was dialyzed in DMSO for 12 h, in deionized water for 24 h, and lyophilized to obtain Ce6-CD.

To prepare Fc-pep-PEG, Fc-pep (0.01 mmol, 10.10 mg) and PEG (0.012 mmol, 12 mg) were dissolved in 2 mL of DMF, and then three equivalents of triethylamine were added to adjust the pH. The product was collected after the reaction at 25 °C for 24 h. Fc-pep-PEG was obtained by dialysis lyophilization in the same way as described above. Both samples were characterized by time-of-flight mass spectrometry, ^{1}H-NMR spectroscopy, and Fourier transform infrared spectroscopy.

Construction and characterization of NPs

Fc-pep-PEG and Ce6-CD were dissolved in DMF and mixed at a molar ratio of 1:1. The mixture was sonicated for 30 min to form a supramolecular clathrate. Then, the solution was mixed with the NLG919 solution, slowly dropped into 15 volumes of deionized water, stirred for 15 min, and processed with an ultrasonic cell disruptor (65 W, 8 min). Finally, the DMF was removed, and the NLG919@CF nanoparticles were concentrated using a centrifugal filter (molecular weight cutoff (MWCO) 10 kDa, Millipore). The particle size distribution, surface ζ potential and polydispersity index (PDI) of NLG919@CF were determined by a particle size analyzer, and its morphology was observed *via* transmission electron microscopy. After 650 nm laser irradiation, the particle size, potential and basic morphology were examined again. The nanoparticles were incubated in 1640 complete medium containing 10% FBS at 37 °C and in pH 7.4 PBS at 4 °C to determine their particle size distribution and surface ζ potential changes, so that we could investigate their stability and storage stability in vitro.

Cellular uptake and retention in vitro

4T1 cells (1×10^5 cells per well) were seeded into 12-well plates and grown for 24 h. Then, free Ce6, CF or NLG919@CF was added to 12-well plates containing the same concentration of Ce6 (1 μg/mL). The medium was removed after incubating for 2–4 h. Afterward, the cells were digested and collected with 0.25% pancreatic enzyme containing 0.02% EDTA, centrifuged and washed with PBS, and then re-suspended in PBS. The intracellular Ce6 fluorescence intensity was detected by flow cytometry. Then, 4T1 cells were incubated by the same

procedure as above and treated with the drug. After incubation, the cells were fixed with 4% paraformaldehyde solution for 30 min. The nuclei were stained with DAPI solution, and the fluorescence signals in the cells were observed under confocal laser microscope.

Furthermore, we investigated the penetration ability of the constructed transformable nanoparticles in tumor spheres. First, 4T1 cells (5×10^3 cells per well) were seeded on a cooled low-melting agar gel, and cultured in an incubator for 5–7 days. MSCs with complete morphology and spherical shapes were marked for later use. Nanoparticles were synthesized and constructed with FITC-labeled PEG. NLG919@CF-FITC was added to the MSCs for incubation. After 4 h, the medium containing the drug was discarded, the cells were washed twice with PBS, and fresh drug-free medium was added. Half of the MSCs were irradiated with a laser (650 nm, 100 mW/cm^2, 20 s), and the others were cultured continuously without treatment. After another 4 h, all the MSCs were washed twice with PBS and fixed. Then, the samples were aspirated and placed on glass slides. The fluorescence signal intensity of FITC at different depths on tomography was observed *via* laser confocal fluorescence microscopy.

ROS generation and cytotoxicity in vitro

ROS experiment: 4T1 cells (1×10^5 cells per well) were inoculated into 12-well plates. Free Ce6, CF, and NLG919@CF (at the same Ce6 concentration of 0.5 μg/mL) were added after 24 h of culture. After administration, the cells were incubated for 6 h. Then half of the wells in each group were irradiated by a laser (650 nm, 100 mW/cm^2, 20 s). All the cells were subsequently cultured continuously for 2 h. Then, the cells were lightly washed twice with PBS, the ROS probe 2′,7′-Dichlorodihydrofluorescein diacetate (DCFH-DA) was added to a final concentration of 10 μM, and the cells were incubated for 20 min. After digestion with pancreatic enzymes, the cells were collected and the fluorescence intensity was measured *via* flow cytometry.

Apoptosis experiments: 4T1 cells (1×10^5 cells per well) were inoculated into 12-well plates. Free Ce6, CF, and NLG919@CF (at the same Ce6 concentration of 0.5 μg/mL) were added after 24 h of culture. Drug-free medium was used as a blank control. After 6 h of incubation, half of the wells in each group were subjected to laser irradiation (650 nm, 100 mW/cm^2, 20 s). All the cells were subsequently cultured for another 2 h. The cells were collected by pancreatic enzyme digestion. Sequentially, Annexin V-FITC and PI staining reagents were added, after which the fluorescence intensity of cells was detected *via* flow cytometry.

Calcein-AM/PI staining experiments: 4T1 cells (1×10^5 cells per well) were inoculated into 12-well plates. Free Ce6 and NLG919@CF (at the same Ce6 concentration of 0.5 μg/mL) were added after 24 h of culture. Drug-free medium was used as a blank control. After 6 h of incubation, half of the wells in each group were subjected to laser irradiation (650 nm, 100 mW/cm^2, 20 s). All the cells were subsequently cultured for another 4 h. After incubation, the cells were stained with Calcein-AM and PI mixture for 30 min and observed under a confocal laser microscope.

MTT experiment: 4T1 cells were seeded in 96-well plates at a density of 5×10^3 cells/well and cultured in an incubator for 24 h. The medium was subsequently replaced with fresh medium, and free Ce6, CF, and NLG919@CF with the same Ce6 concentrations were added (5 μg/mL, 2.5 μg/mL, 1.25 μg/mL, 0.625 μg/mL, 0.3125 μg/mL and 0.156 μg/mL). The mixture was incubated for another 4 h. Half of the plates in each group were irradiated by a laser (650 nm, 100 mW/cm^2, 20 s), and incubation was continued for 20 h. After the end of the incubation, a medium containing 0.5 mg/mL MTT was added for another 4 h. The liquid was aspirated from the wells of the plates, 100 μL of dimethyl sulfoxide was added to each well and mixed thoroughly to dissolve the formazan. The absorbance was determined at 490 nm using a microplate reader.

ICD induction in vitro

The cell culture and dosing regimens used were the same as those in the ROS experiments. After incubation, tests were performed using the ATP Kit and HMGB-1 Kit according to the manufacturer's instructions. After the cells were digested by pancreatic enzymes and incubaμted with CRT antibodies on ice for 30 min, CRT efflux was measured by flow cytometry and immunofluorescence staining.

Biodistribution and retention evaluation in vivo

Female BALB/c mice and BALB/c nude mice were subjected to adaptive feeding 7 days before modeling. On Day 8, the breast cancer model was established. After anesthesia, 3×10^5 4T1 cells were injected into the left third breast pad of the mouse. The next experiment was conducted when the tumor size reached to approximately 200mm^3.

First, an in vivo tissue distribution experiment was performed. BALB/c mice with similar tumor volumes were selected and randomly divided into 2 groups ($n=3$). Free Ce6 and CF (at the same Ce6 concentration of 2 mg/kg) were injected through the tail vein. In vivo fluorescence imaging (Ex 640 nm, Em 710 nm) was performed at 2, 4, 8, 12, and 24 h after injection *via* a Lumina III Imaging System (PerkinElmer, USA). Twenty-four hours later, all the mice were dissected, and the heart, liver, spleen, lung, kidney and tumor tissues were harvested. These tissues were washed with PBS and fixed in 4% paraformaldehyde.

Subsequently, fluorescence imaging was performed using the same imaging system, and semiquantitative analysis was performed *via* statistical analysis of the fluorescence intensity *via* live imaging software.

Then, we investigated the retention of the nanoparticles in tumors. BALB/c nude mice with similar tumor volumes were selected and randomly divided into 2 groups ($n=3$). All the mice were intratumorally injected with CF-FITC; one group was immediately subjected to laser irradiation at the tumor site (650 nm, 200 mW/cm^2, 5 min); and In vivo fluorescence imaging was performed at 10 min, 2 h, 4 h, 8 h, 12 h and 24 h after injection. The remaining steps were the same as above.

Antitumor therapy

First, a mouse model of breast cancer and bone metastasis was constructed. 4T1 cells (3×10^5) were injected into the left third breast pad, and 1.5×10^5 4T1 cells were injected into the right tibia of mice at the same time after anesthesia. When the tumor volume in situ reached approximately 60 mm^3, the mice were randomly divided into 7 groups ($n=5$): the PBS group, free NLG919 group, anti-PD-1 group, NLG919@CF group, CF+L group, NLG919@CF+L group and NLG919@CF+L+anti-PD-1 group (the Ce6 concentration was 4 mg/kg, and the NLG919 concentration was 2.4 mg/kg). The corresponding preparations were injected into the mice through the tail vein. In the laser irradiation group, the primary tumor was irradiated (650 nm, 200 mW/cm^2, 5 min) by a laser after 12 h of administration. Anti-PD-1 antibody (100 μg per mouse) was intraperitoneally injected 24 h after laser irradiation. Treatment was administered every 3.5 days for a total of 4 cycles. The tumor sizes and body weights of the mice were recorded every 2 days beginning on Day 8. Twenty days after the establishment of the tumor model, the mice were sacrificed, and the tumors in situ and bone tumors were collected, weighed, photographed, sectioned, and stained. At the same time, the heart, liver, spleen and kidney of mice in each group were collected for H&E staining to evaluate the pathological changes in the main organs. We collected lung tissue and evaluated lung metastases under magnification. Moreover, H&E staining was performed to evaluate the lung metastases in each group.

Immune effect

First, the maturation of DCs in mice was investigated. After the mice were sacrificed, their spleens and lymph nodes were extracted, sectioned, carefully ground, centrifuged and washed to prepare a single-cell suspension. After staining with anti-CD11c-FITC, anti-CD80-PE/Cy7 and anti-CD86-APC antibodies, the samples were analyzed *via* flow cytometry.

Subsequently, we investigated the infiltration of T cells into tumors. In situ tumor tissues were collected, cut and placed in PBS solution. DNase, collagenase IV and Haase were added to concentrations of 30 U/mL, 175 U/mL and 100 U/mL, respectively, and then incubated at 37 °C for 45 min. Single-cell suspensions were prepared by filtration, centrifugation and washing, and then stained with anti-CD3-APC/Cy7, anti-CD4-FITC, anti-CD8-APC, and anti-Foxp3-PE. CTLs ($CD3^+CD8^+$) and Tregs ($CD3^+CD4^+$ $Foxp3^+$) were analyzed *via* flow cytometry.

Micro-CT

After the mice were sacrificed, the tibias were detached, soaked in 4% paraformaldehyde and fixed for 48 h. Changes in tibia bone mass were detected by micro-computed tomography (Micro-CT, PerkinElmer, Quantum GX II, USA) at 90 kV and 88 μA with a voxel size of 72 μm. Bone volume was analysed using the whole tibia of each mouse as the ROI.

Statistical analysis

All the data are reported as the mean ± standard deviation or mean ± standard error of at least three samples. One-way ANOVA was used for multiple comparisons and statistical analysis was performed using GraphPad PRISM 8 software. $P<0.05$ was considered to indicate statistical significance.

Conclusion

In summary, we report a transformable self-delivered supramolecular nanomedicine, constructed by host-guest interactions between Fc and β-CD that can be loaded with the IDO-1 inhibitor NLG919. In the present study, PDT combined with immunotherapy was used to treat breast cancer with bone metastases effectively. This protocol has several advantages. First, our constructed NLG919@CF nanoparticles have an EPR effect, which can increase the targeting potential of the drug for tumor aggregation. After reaching the tumor, the nanoparticles can be transformed into nanofibers upon laser irradiation, which enhances their retention. In addition, the self-delivering nanodrug delivery system constructed in this study requires no additional carrier, which prevents the potential biotoxicity of nanomaterials. Finally, PDT combined with immunotherapy can ameliorate immunosuppression in the tumor microenvironment, reduce the number of Tregs and restore the viability of CTLs. It can effectively treat breast cancer with bone metastases and inhibit osteolysis. This study provides ideas and directions for exploring new treatment strategies for bone metastasis in patients with breast cancer.

Supplementary Information

The online version contains supplementary material available at https://doi.org/10.1186/s12951-024-02839-0.

Supplementary Material 1

Acknowledgements
The Scheme 1 were assisted by Figdraw (https://www.figdraw.com).

Author contributions
Yi Qin, Huile Gao and Xueying Liu designed the research. Xueying Liu carried out the experiment with assistance of Jiamei Li, Zhaofeng Li and Siqin He. Xueying Liu prepared figures with assistance of Hao Wang, Chuan Hu and Yujun Song. Xueying Liu wrote mainly the manuscript and Huile Gao assisted with the manuscript reviewing. Yi Qin provided the funding. All authors reviewed the manuscript.

Funding
This work was supported by National Natural Science Foundation of China (82174142), Supporting Project of Natural Science Foundation of China (PT8217140653), Zhuhai Xiangshan Talent Project (2021XSYC-01), Zhuhai Public Hospital Comprehensive Reform Project (YC202303).

Data availability
Data will be made available on request.

Declarations

Ethics approval and consent to participate
All animal experiments were performed under the guidelines, evaluated and approved by the ethics committee of Sichuan University.

Consent for publication
All participants consented to publish the paper.

Competing interests
The authors declare no competing interests.

Author details
[1]Department of Orthopedics, Zhuhai People's Hospital (Zhuhai Clinical Medical College of Jinan University), Zhuhai 519000, China
[2]Key Laboratory of Drug Targeting and Drug Delivery Systems, West China School of Pharmacy, Sichuan University, Chengdu 610041, China
[3]Department of Breast, Sichuan Clinical Research Center for Cancer, Sichuan Cancer Hospital & Institute, Sichuan Cancer Center, Affiliated Cancer Hospital of University of Electronic Science and Technology of China, Chengdu 610000, China

Received: 1 April 2024 / Accepted: 5 September 2024
Published online: 14 September 2024

References

1. Siegel RL, Miller KD, Wagle NS, Jemal A. Cancer statistics, 2023. Cancer J Clin. 2023;73:17–48.
2. Ording AG, Heide-Jørgensen U, Christiansen CF, Nørgaard M, Acquavella J, Sørensen HT. Site of metastasis and breast cancer mortality: a Danish nationwide registry-based cohort study. Clin Exp Metastasis 2017, 34.
3. Zhang W, Bado IL, Hu J, Wan Y-W, Wu L, Wang H, Gao Y, Jeong H-H, Xu Z, Hao X et al. The bone microenvironment invigorates metastatic seeds for further dissemination. Cell 2021, 184.
4. Li Z, Zhang W, Zhang Z, Gao H, Qin Y. Cancer bone metastases and nanotechnology-based treatment strategies. Expert Opin Drug Deliv. 2022;19:1217–32.
5. Liu Y-Q, Wang X-L, He D-H, Cheng Y-X. Protection against chemotherapy- and radiotherapy-induced side effects: a review based on the mechanisms and therapeutic opportunities of phytochemicals. Phytomedicine: Int J Phytotherapy Phytopharmacology. 2021;80:153402.
6. Nadella KR, Kodali RM, Guttikonda LK, Jonnalagadda A. Osteoradionecrosis of the Jaws: Clinico-Therapeutic Management: A literature review and update. J Oral Maxillofac Surg. 2015;14:891–901.
7. Kwiatkowski S, Knap B, Przystupski D, Saczko J, Kędzierska E, Knap-Czop K, Kotlińska J, Michel O, Kotowski K, Kulbacka J. Photodynamic therapy - mechanisms, photosensitizers and combinations. Biomed Pharmacotherapy = Biomedecine Pharmacotherapie. 2018;106:1098–107.
8. Fang H, Gai Y, Wang S, Liu Q, Zhang X, Ye M, Tan J, Long Y, Wang K, Zhang Y, Lan X. Biomimetic oxygen delivery nanoparticles for enhancing photodynamic therapy in triple-negative breast cancer. J Nanobiotechnol. 2021;19:81.
9. Yang Y, Zhu W, Feng L, Chao Y, Yi X, Dong Z, Yang K, Tan W, Liu Z, Chen M. G-Quadruplex-based Nanoscale Coordination polymers to modulate Tumor Hypoxia and Achieve Nuclear-targeted drug delivery for enhanced photodynamic therapy. Nano Lett. 2018;18:6867–75.
10. Lan G, Ni K, Xu Z, Veroneau SS, Song Y, Lin W. Nanoscale Metal-Organic Framework overcomes Hypoxia for photodynamic therapy primed Cancer Immunotherapy. J Am Chem Soc. 2018;140:5670–3.
11. Wu L, Cai X, Zhu H, Li J, Shi D, Su D, Yue D, Gu Z. PDT-Driven highly efficient intracellular delivery and controlled release of CO in combination with sufficient singlet oxygen production for synergistic anticancer therapy. Adv Funct Mater. 2018;28:1804324.
12. He X, Xu C. Immune checkpoint signaling and cancer immunotherapy. Cell Res. 2020;30:660–9.
13. Feng B, Hou B, Xu Z, Saeed M, Yu H, Li Y. Self-amplified drug delivery with light-inducible nanocargoes to Enhance Cancer Immunotherapy. Adv Mater (Deerfield Beach Fla). 2019;31:e1902960.
14. Shemi A, Khvalevsky EZ, Gabai RM, Domb A, Barenholz Y. Multistep, effective drug distribution within solid tumors. Oncotarget. 2015;6:39564–77.
15. Yu W, Liu R, Zhou Y, Gao H. Size-tunable strategies for a Tumor targeted Drug Delivery System. ACS Cent Sci. 2020;6:100–16.
16. Jia W, Wang Y, Liu R, Yu X, Gao H. Shape transformable strategies for drug delivery. Adv Funct Mater. 2021;31:2009765.
17. Bellat V, Ting R, Southard TL, Vahdat L, Molina H, Fernandez J, Aras O, Stokol T, Law B. Functional peptide nanofibers with unique tumor targeting and enzyme-Induced Local Retention properties. Adv Funct Mater. 2018;28:1803969.
18. Cabral H, Matsumoto Y, Mizuno K, Chen Q, Murakami M, Kimura M, Terada Y, Kano MR, Miyazono K, Uesaka M, et al. Accumulation of sub-100 nm polymeric micelles in poorly permeable tumours depends on size. Nat Nanotechnol. 2011;6:815–23.
19. Liu R, Yu M, Yang X, Umeshappa CS, Hu C, Yu W, Qin L, Huang Y, Gao H. Linear chimeric triblock molecules self-assembled micelles with Controllably Transformable Property to Enhance Tumor Retention for Chemo-Photodynamic therapy of breast Cancer. Adv Funct Mater. 2019;29:1808462.
20. Qin Y, Tong F, Zhang W, Zhou Y, He S, Xie R, Lei T, Wang Y, Peng S, Li Z, et al. Self-delivered supramolecular nanomedicine with transformable shape for Ferrocene-amplified photodynamic therapy of breast Cancer and bone metastases. Adv Funct Mater. 2021;31:2104645.
21. Liu R, An Y, Jia W, Wang Y, Wu Y, Zhen Y, Cao J, Gao H. Macrophage-mimic shape changeable nanomedicine retained in tumor for multimodal therapy of breast cancer. J Controlled Release: Official J Controlled Release Soc. 2020;321:589–601.
22. Li W, Yang J, Luo L, Jiang M, Qin B, Yin H, Zhu C, Yuan X, Zhang J, Luo Z, et al. Targeting photodynamic and photothermal therapy to the endoplasmic reticulum enhances immunogenic cancer cell death. Nat Commun. 2019;10:3349.
23. Huang C, Lin B, Chen C, Wang H, Lin X, Liu J, Ren Q, Tao J, Zhao P, Xu Y. Synergistic reinforcing of immunogenic cell death and transforming Tumor-Associated macrophages Via a multifunctional Cascade Bioreactor for Optimizing Cancer Immunotherapy. Adv Mater (Deerfield Beach Fla). 2022;34:e2207593.
24. Zhang S, Wang J, Kong Z, Sun X, He Z, Sun B, Luo C, Sun J. Emerging photodynamic nanotherapeutics for inducing immunogenic cell death and potentiating cancer immunotherapy. Biomaterials. 2022;282:121433.
25. Chen R, Kang R, Tang D. The mechanism of HMGB1 secretion and release. Exp Mol Med. 2022;54:91–102.

26. Li Z, Liu P, Chen W, Liu X, Tong F, Sun J, Zhou Y, Lei T, Yang W, Ma D, et al. Hypoxia-cleavable and specific targeted nanomedicine delivers epigenetic drugs for enhanced treatment of breast cancer and bone metastasis. J Nanobiotechnol. 2023;21:221.

Publisher's note